

RESEARCH ARTICLE

10.1002/2013JC009488

Mixing dynamics at the confluence of two large rivers undergoing weak density variations

Cintia L. Ramón¹, Joan Armengol², Josep Dolz³, Jordi Prats^{4,5}, and Francisco J. Rueda¹

Key Points:

- Mixing rates in river confluences are sensitive to weak river-density contrasts
- Mixing rates increase up to 40% in response to density contrasts of $O(0.1) \text{ kg m}^{-3}$
- Channel planform and density contrasts control the area available for mixing

Correspondence to:

C. L. Ramón,
crcasanas@ugr.es

Citation:

Ramón, C. L., J. Armengol, J. Dolz, J. Prats, and F. J. Rueda (2014), Mixing dynamics at the confluence of two large rivers undergoing weak density variations, *J. Geophys. Res. Oceans*, 119, 2386–2402, doi:10.1002/2013JC009488.

Received 3 OCT 2013

Accepted 19 MAR 2014

Accepted article online 25 MAR 2014

Published online 14 APR 2014

¹Department of Civil Engineering and Water Research Institute, University of Granada, Granada, Spain, ²Department of Ecology, University of Barcelona, Barcelona, Spain, ³Department of Hydraulic, Ocean and Environmental Engineering, Technical University of Catalonia, Barcelona, Spain, ⁴National Research Institute of Science and Technology for Environment and Agriculture (IRSTEA), Aix-en-Provence, France, ⁵Flumen Institute, Technical University of Catalonia, Barcelona, Spain

Abstract Simulations of tracer experiments conducted with a three-dimensional primitive-equation hydrodynamic and transport model are used to understand the processes controlling the rate of mixing between two rivers (Ebro and Segre), with distinct physical and chemical properties, at their confluence, upstream of a meandering reservoir (Ribarroja reservoir). Mixing rates downstream of the confluence are subject to hourly scale oscillations, driven partly by changes in inflow densities and also as a result of turbulent eddies that develop within the shear layer between the confluent rivers and near a dead zone located downstream of the confluence. Even though density contrasts are low—at most $O(10^{-1}) \text{ kg m}^{-3}$ difference among sources—and almost negligible from a dynamic point of view—compared with inertial forces—they are important for mixing. Mixing rates between the confluent streams under weakly buoyant conditions can be of up to 40% larger than those occurring under neutrally buoyant conditions. The buoyancy effects on mixing rates are interpreted as the result of changes in the contact area available for mixing (distortion of the mixing layer). For strong density contrasts, though, when the contact area between the streams becomes nearly horizontal, larger density differences between streams will lead to weaker mixing rates, as a result of the stabilizing effect of vertical density gradients.

1. Introduction

River confluences are critical points in river networks where strong physical and chemical gradients develop [Kiffney *et al.*, 2006; Bigelow *et al.*, 2007; Gooseff *et al.*, 2008], resulting in a wide range of distinctive environmental conditions (habitats) for biological growth. As a consequence, river confluences behave as biological hotspots, where the number of species appears to increase very significantly in comparison with other river reaches [Benda *et al.*, 2004]. The effects of river confluences persist downstream, hence, affecting biological communities and ecological processes at scales of river reaches and channel networks [Rice *et al.*, 2001]. The spatial extent of the reaches downstream of river junctions where heterogeneous habitat conditions persist largely depends on the rate at which fluid elements are exchanged across the mixing interface separating mainstream and tributary waters. Mixing rates are largely dependent on the development of two-dimensional vortices in the shear layer between the confluent flows, and, particularly, on processes leading to the distortion of the mixing layer and the consequent increase in the area of contact between water masses. The distortion of the mixing layer, in turn, has been shown to occur as a result of differences in depths between the main channel and the tributary (bed discordance) or channel-scale helical motions, which, in general, result in significant reductions in mixing lengths [e.g., Gaudet and Roy, 1995; Rhoads and Kenworthy, 1995]. Lane *et al.* [2008], for example, found that mixing lengths between the Paraná and Paraguay rivers can vary from ca. 8 to 400 km depending on whether helical motions develop or not. Farther downstream of the confluence, mixing rates largely depend on the local characteristics of the channel [Boxall and Guymer, 2001; Heard *et al.*, 2001], such as the presence of channel bends where strong secondary currents develop, or on the existence of dead zones, such as pools, gravel beds, side arms, or, in general, any other irregularity in the river morphology.

Our understanding of flow and mixing dynamics in river confluences, however, is still far from complete. In particular, the effect on mixing of the density contrast between the confluent streams have been traditionally neglected, which has been justified by differences in the inertia of the confluent flows being much

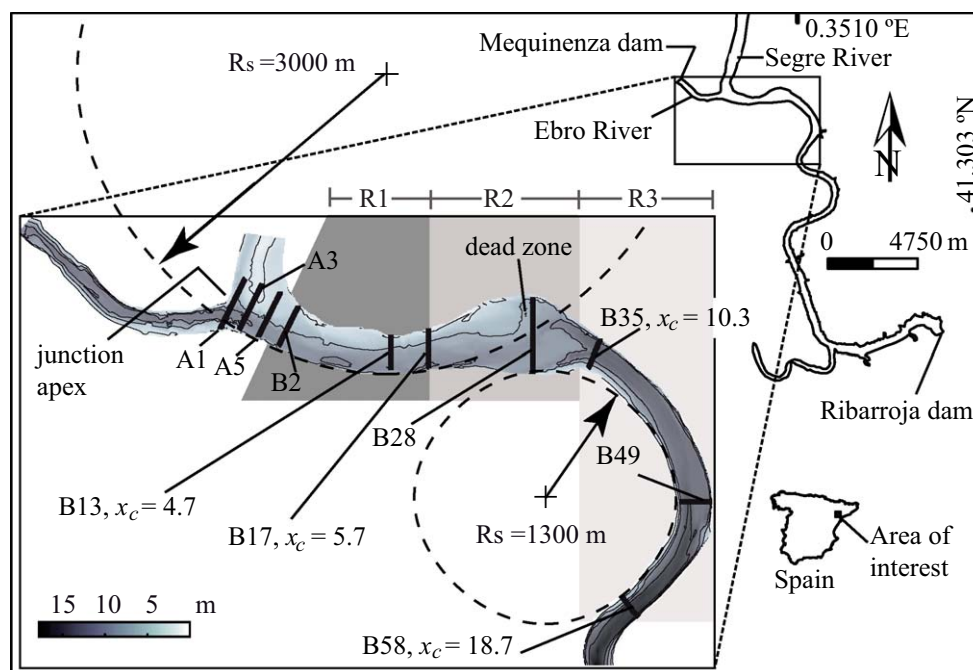


Figure 1. Ribarroja reservoir and bathymetry of the computational domain (rectangle). The location of sections A1, A3, and A5 at the confluence region, the location of some of the B sections downstream of the confluence region, and the location of the dead zone are also shown. x_c is the nondimensional distance downstream of the junction apex. R_s = radius of curvature. Shaded areas show the extension of reaches R1, R2 and R3.

higher than density differences [e.g., Rhoads, 1996]. Laraque *et al.* [2009], in their field study of the confluence between the Negro and Solimões rivers, however, argued that the small density differences, associated with slight changes in suspended solid concentrations, made the waters from the Negro River to flow over those of the Solimões River, widening and distorting the mixing layer, and, hence, increasing mixing rates. These density differences, in general, are more likely to occur in large-scale confluent channels, with the mainstream and tributary draining different geological terrains [Parsons *et al.*, 2008]. They could also be the result of differences in the thermal inertia between the mainstream and the tributary, and, in this case, one would expect the temperature-driven variations in density to occur at hourly scales, as a result of diurnal variations in insolation. The contribution of small density differences to mixing dynamics in confluences has not been addressed before, with the exception of the numerical study of Biron and Lane [2008] in a simplified 90° junction of two rectangular channels with density differences of $O(1) \text{ kg m}^{-3}$. In that study, Biron and Lane [2008] demonstrated that mixing rates increased if the mixing layer distorted as a result of density differences. It is not clear, however, whether weaker or stronger density differences, or hourly scale variations in density, will have an effect or not on the mixing rates in river confluences.

Our goal is to understand the effects of density differences on the mixing dynamics in and downstream of large-scale asymmetric confluences. The junction of two medium-size rivers (Ebro and Segre) in northern Spain is used as an example of a large confluence with weak and time-varying density differences, driven by diurnal changes in water temperatures [Ramón *et al.*, 2013]. The two rivers join at the upstream end of a meandering reservoir (Ribarroja) with a complex geometry characterized by bed discordance and changes in channel geometry and planform occurring sequentially (Figure 1). Hence, mixing rates between the confluent rivers are expected to exhibit changes both in time and downstream of the confluence along the river channel. We analyze those changes through simulations conducted with a three-dimensional primitive-equation (3-D-PE) model. Our modeling approach is justified given the need to conduct unsteady simulations of density-driven changes [Ramón *et al.*, 2013] in the mixing layer between two water masses in a large domain with a reasonable computational cost. The 3-D-PE models have been successfully applied, during the last few years, to reproduce and analyze space-time changes of density interfaces in large-scale systems, during periods of time of days to years with reasonable computational cost. For example, they

have been used to simulate the dynamics of salt wedges in estuaries [Robson and Hamilton, 2004] or the internal wavefields and mixing across pycnoclines in lakes and reservoirs [Hodges et al., 2000; Rueda et al., 2003; Vidal et al., 2007]. In the particular case of the confluence between the Ebro (hereon western W-River) and Segre (hereon northern N-River) rivers, the large spatial scales of the domain of interest (see Figure 1) and the need to account for the variability of the density changes at hourly scales prevent the use of more sophisticated modeling approaches, such as well-resolved Large Eddy Simulations (LES) [Rodi, 2010]. Even the hybrid Reynolds-Averaged Navier Stokes (RANS)-LES approach of Constantinescu et al. [2011, 2012] is too computationally costly and not viable. For their RANS-LES simulation of the small river confluence between the KasKaskia and Copper Slough rivers, for example, Constantinescu et al. [2011, 2012] used a total of $\sim 5 \times 10^6$ cells to discretize the ~ 52 m length and ~ 8 m width computational domain and they could only simulate steady state conditions. Our unsteady simulations, however, require time scales of $O(10^5)$ time steps, which far exceed the $O(10^4)$ time steps required to reach equilibrium. RANS models are alternative to LES models to conduct unsteady simulations, providing reasonable and cost-effective results. Biron et al. [2004], for example, used RANS models to simulate the downstream evolution of mixing between the Bayonne and Berthier rivers and were able to reproduce the field observations collected by Gaudet and Roy [1995]. Still, full 3-D RANS models based on nonhydrostatic equations are very demanding, and the additional simplifications of the governing equations incorporated in the 3-D-PE are needed. The ability of 3-D-PE models to simulate relevant physical processes in river mixing and dynamics has been recently analyzed by C. L. Ramón et al. (Validation of a Cartesian 3D free surface hydrodynamic model for simulating turbulent flows in the confluence of two rivers entering a meandering reservoir, submitted to *International Journal of Computational Methods*, 2013). Their results suggest that 3-D-PE models, although approximate and hence less expensive than more sophisticated approaches, yield solutions which are consistent with experimental observations.

The present study is distinctive in several important aspects. First and most important, the influence of weak density differences on mixing dynamics is taken into account. Given the paucity of publications on this topic, we believe that this is an important contribution. Second, the computational domain extends ~ 8 km downstream of the confluence so the streamwise variability of mixing rates can be evaluated. Few studies have extended their analysis farther downstream of the confluence, but those that have, suggest that different phenomena may have different contributions to mixing depending on flow rates. For instance, Biron et al. [2004] suggest that for the Bayonne-Berthier confluence, the effect of bed discordance is particularly pronounced during low flow conditions, while the effect of river bending farther downstream of the confluence appears to be stronger during high flow conditions. Hence, mixing rates are expected to vary in space which supports our analysis in the downstream reach of the confluence.

2. Study Site

Ribarroja reservoir ($41^\circ 18'N$, $0^\circ 21'E$) is the second of a chain of three reservoirs (Mequinenza-Ribarroja-Flix) constructed along the lower reaches of the W-River for hydroelectric power generation. The basin is relatively shallow, with an average depth of 9.8 m, reaching values of up to 34 m near the dam. Inflows and outflows are regulated so that the free surface elevation is kept at a nearly constant value of ca. 70 m above sea level throughout the year. During peak through flows in winter, the nominal residence time of the reservoir can be as low as 3 days [Cruzado et al., 2002]. The reservoir has an elongated and meandering shape (Figure 1), with the two largest inflows (W-River and N-River) occurring at the NW end. The river confluence is characterized by a large (near 90°) junction angle and a curved planform which bends to the left immediately downstream of the confluence with a radius of curvature R_s of ca. 3 km, almost 7 times the channel width b_p downstream of the confluence, $R_s/b_p \sim 7.5$ (Figure 1, reach R1). Depths of the W-River and N-River are discordant: the N-River enters the confluence through two channels of depths D of 4 and 6 m, respectively, while depths encountered at the W-River are of ~ 10 m. Downstream of reach R1, the channel widens as it veers to the right, leaving a wide shallow embayment on the left margin (reach R2). Finally, in reach R3, the channel bends sharply to the right with a radius of curvature R_s ca. 1.3 km ($R_s/b_p \sim 3.25$; Figure 1). Inflows from the W-River are regulated by Mequinenza dam, which discharges directly into Ribarroja reservoir 3 km upstream of the confluence. Only the hydroelectric intake, releasing deep cold hypolimnetic water, and the spillway in Mequinenza dam are operated on a regular basis [Prats et al., 2010].

Table 1. Model Inputs for the Simulation Runs

Run Case	$\Delta\rho/\rho_0^a$	Q_W^b ($\text{m}^3 \text{s}^{-1}$)	Q_N^b ($\text{m}^3 \text{s}^{-1}$)	$R_q (=Q_N/Q_W)$	R_M^c
Base	3.6×10^{-5} to 1.2×10^{-4}	730	96	0.13	0.03
T1	2.4×10^{-4}	730	96	0.13	0.03
T2	1.5×10^{-4}	730	96	0.13	0.03
T3	6.8×10^{-5}	730	96	0.13	0.03
T4	3.2×10^{-5}	730	96	0.13	0.03
T5	0	730	96	0.13	0.03
T6	-6.8×10^{-5}	730	96	0.13	0.03
T7	-1.5×10^{-4}	730	96	0.13	0.03
T8	-2.4×10^{-4}	730	96	0.13	0.03
M1	1.5×10^{-4}	500	326	0.65	0.72
M2	6.8×10^{-5}	500	326	0.65	0.72
M3	0	500	326	0.65	0.72
M4	-6.8×10^{-5}	500	326	0.65	0.72
M5	-1.5×10^{-4}	500	326	0.65	0.72
m1	1.5×10^{-4}	326	500	1.53	4.58
m2	6.8×10^{-5}	326	500	1.53	4.58
m3	0	326	500	1.53	4.58
m4	-6.8×10^{-5}	326	500	1.53	4.58
m5	-1.5×10^{-4}	326	500	1.53	4.58

^aDensity contrast ($\Delta\rho = \rho_W - \rho_N$) between the Ebro (ρ_W) and Segre (ρ_N) rivers expressed in terms of a reference density ($\Delta\rho/\rho_0$).
^bInflow rates Q ($\text{m}^3 \text{s}^{-1}$) for the Ebro (Q_W) and the Segre (Q_N) rivers.
^cMomentum ratio between the Ebro and Segre rivers ($=Q_N \times u_N \times \rho_N / (Q_W \times u_W \times \rho_W)$), u_N and u_W being the mean streamwise velocities of the Segre and Ebro rivers, respectively, immediately upstream of their confluence.

3. Methods

3.1. Approach

The model was first used to simulate the flow fields in the confluence during a period of time in February 2009, when experimental observations are available [Ramón *et al.*, 2013]. At that time, conductivity differences between rivers were of $\sim 80 \mu\text{S cm}^{-1}$ and river temperatures varied weakly (at most 1°C) in time, so that density differences between rivers ranged from $O(10^{-2})$ to $O(10^{-1}) \text{ kg m}^{-3}$ with the W-River being denser. Inflow rates were constant, but almost 8 times larger from the W-River (Q_W) than from the side inflows along the N-River (Q_N). This simulation corresponds to the *base case (Base)* in Table 1 and was used by C. L. Ramón *et al.* (submitted manuscript, 2013) for validation purposes. Additional simulations were conducted in this work with different inflow densities and discharge ratios $R_q (=Q_N/Q_W)$, both constant in time (Table 1). Runs T1 through T8 refer to those simulations conducted with different density contrasts between the W- (ρ_W) and N- (ρ_N) rivers, but setting the inflow rates equal to the observations. The density contrast $\Delta\rho/\rho_0$ is defined as $(\rho_W - \rho_N)/\rho_0$, where $\rho_0 (= 1000 \text{ kg m}^{-3})$ is a reference density. Hence, $\Delta\rho/\rho_0 > 0$ will refer to scenarios with positively buoyant side inflows. Runs M1–M5 and m1–m5 refer to those simulations conducted both with different $\Delta\rho/\rho_0$ and R_q (Table 1). M-simulations and m-simulations correspond to $R_q = 0.65$ (momentum ratio $R_M = 0.72$) and 1.53 ($R_M = 4.58$), respectively. In all M-simulations and m-simulations total discharge was equal to that observed in the field, so that the influence of R_q could be compared. The selection of the values of R_q of 0.65 and 1.53 was intended to include situations in which inflows from the W-River are still dominant but R_q is closer to 1, and the reversed situation, in which the N-River dominates the flow. All discharge ratios are within the range of variation of R_q observed in Ribarroja under weakly stratified conditions [e.g., Ramón *et al.*, 2013]. The simulated velocity fields for the different scenarios were used to drive transport simulations in which the W-inflows were traced as they entered into the computational domain. The results of the hydrodynamic and transport models were analyzed to understand the processes driving mixing at and downstream of the junction.

3.2. Computational Model

Simulations were conducted with a parallel version [Acosta *et al.*, 2010] of a 3-D-PE model [Smith, 2006]. The governing equations are first posed in layer-averaged form by integrating over the height of a series of horizontal layers separated by level planes. The layer-averaged momentum equations are solved using a semi-implicit, three-level, iterative leapfrog-trapezoidal finite difference scheme on a staggered Cartesian grid. Nonactive (i.e., tracers) and active scalar transport equations were solved using a two-level semi-implicit

scheme, in which only vertical diffusion is discretized implicitly. The advection terms in the transport equation for scalars are discretized with a second-order accurate flux-limiting scheme [e.g., Durran, 1999] with use of the Superbee limiter [Roe, 1984]. Turbulent mixing is represented in the 3-D model using diffusion-like terms. A Laplacian operator with constant mixing coefficients (K_h) is used to represent horizontal mixing of momentum and scalars. Vertical eddy coefficients of mixing K_z are calculated using a two-equation model originally proposed by Mellor and Yamada [1974]. This turbulent modeling approach is typically used in large-scale models for geophysical flows due to their reduced computational burden. The model has been extensively validated both against analytical solutions and field data sets collected in a variety of lake environments [Rueda and Cowen, 2005; Rueda and MacIntyre, 2010, and references therein] and estuaries [Zamani et al., 2010]. The model was also validated for relevant physical processes occurring in the confluence between the W-River and N-River (C. L. Ramón et al., submitted manuscript, 2013). Those processes include (1) the development of a shallow mixing layer between two confluent streams, (2) flow past a cavity, and (3) flow in open channels of mild curvature with and without stratification. R. L. Ramón et al. (submitted manuscript, 2013) also validated the model results against field data (*base case*, Table 1).

3.3. Transport and Mixing Model of Ribarroja Reservoir

Our computational domain extends from Mequinenza dam to a section existing ca. 8 km downstream of the junction (Figure 1) along the W-River, and approximately 500 m upstream of the confluence along the N-River. The lake geometry was discretized using grid cells of size $(\Delta x, \Delta y, \Delta z) = (10, 10, 0.5)$ m in the longitudinal, lateral, and vertical direction, respectively. The time step Δt was set to 2 s for stability purposes. The bottom drag coefficient, C_d , was set to 0.003 as proposed by Smith [2006]. The horizontal mixing coefficient K_h was set to $5 \times 10^{-2} \text{ m}^2 \text{ s}^{-1}$. This estimate corresponds to the product of the friction velocity $u^* (= C_d^{0.5} U$, U being the cross-sectional averaged streamwise velocity) and the channel depth D , as proposed by Rastogi and Rodi [1978] to quantify turbulent transfer of momentum and temperature. The values of u^* and D were, in turn, estimated from field data ($U = 0.4 \text{ m s}^{-1}$ and $D = 10 \text{ m}$; Ramón et al. [2013]). Preliminary simulations showed, however, that the actual value of K_h can be ignored for advection of scalars, since changes in mixing rates of at most 4% occurred in response to decreases in K_h from 10^{-2} to $0 \text{ m}^2 \text{ s}^{-1}$. The model was set to run using a second-order space-centered method for momentum advection and two trapezoidal iterations after the initial nonsmoothed leapfrog predictive step.

The reservoir was assumed initially at rest with a uniform density, equal to the averaged density of the W-River and N-River. At the downstream end, the free surface elevation was fixed, with densities and tracer concentrations having zero gradients. Inflow rates and densities at the upstream boundaries, in turn, were set to follow the field data of Ramón et al. [2013]. Inflow rates from the W-River were set to a constant value of $730 \text{ m}^3 \text{ s}^{-1}$ and were distributed uniformly in the inflow section. Inflows from the N-River were also constant but assumed to occur through two sections with different velocities, as observed in the field. Almost 2/3 of the total inflow rate ($96 \text{ m}^3 \text{ s}^{-1}$) from the N-River was presumed to enter through the main channel ($66 \text{ m}^3 \text{ s}^{-1}$) and the remaining through the secondary channel. Inflow temperatures were allowed to vary in time, with the hourly variations within any given day of the simulation following the observations collected on day 50 (2009). Wind forcing was weak at the time of the experiments [Ramón et al., 2013] and was assumed negligible in the model. The model was run until more than 99% of the tracer mass initially existing in the domain has left (approximately 9 days).

3.4. Tracer Experiment and Mixing Rates

W-water was traced using a constant tracer concentration $C_w = 100$ ppm. The tracer concentrations downstream, varying from 0 to 100, indicated the percentage of W-water in the mixture and, hence, were used to establish the level of mixing between the W-River and N-River. Mixing ratios were evaluated each 0.25 h at 58 cross sections downstream of the confluence (cross sections B1–B58, Figure 1). The distance between consecutive B sections was ca. 120 m, and the last section was almost 1 km from the downstream boundary to avoid the influence of boundary conditions. Other simulations (not shown) were conducted with the downstream boundary displaced 1.5 km farther downstream, with estimates of mixing rates at section 58 which varied less than 1% with respect to the reference case. We will use the symbol x_c to refer to the distance downstream of the junction apex of each of these cross sections and will be given as a multiple of b_p . Two different approaches proposed by Biron et al. [2004] were used to quantify mixing levels. The first is

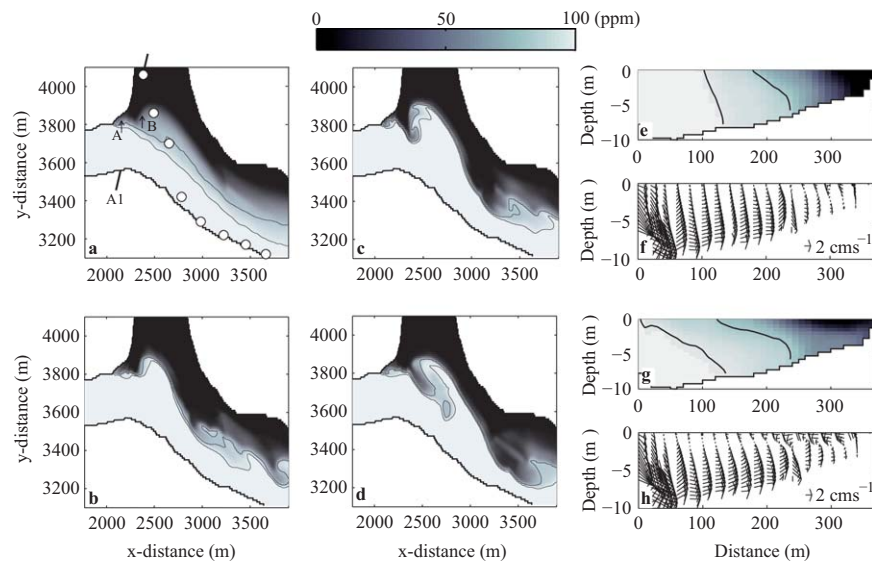


Figure 2. (a) Time-averaged and (b–d) instant tracer concentrations at the surface plane; (Figure 2b) 19:00 h, (Figure 2c) 19:15 h, and (Figure 2d) 19:30 h. Time-averaged (e and g) tracer concentration (ppm) and (f and h) lateral velocities in section B13 ($x_c = 4.7$) between (Figure 2e and 2f) 11–12 h and (Figure 2g and 2h) 19–20 h. Distance = 0 m at the right bank. Black solid lines in Figures 2a–2e and 2g account for the location of the mixing interface ($=C_p \pm 10\%$) and white dots in Figure 2a show the location of the maximum time-averaged water surface elevation in sections A1 ($x_c = 0.17$) to B12 ($x_c = 4.4$). Arrows in Figure 2a show the locations—stagnation zone A and mixing layer B—where the spectral signal of the velocity fluctuations was calculated in Figures 4c and 4d. Run case *base* in Table 1.

based on an index referred to as deviation from complete mixing δ [Gaudet and Roy, 1995]. For a given cell, i , in a cross section, the deviation from complete mixing δ was calculated as follows:

$$\delta(i) = \frac{C(i) - C_p}{C_p} \times 100 \tag{1}$$

where $C(i)$ is the simulated tracer concentration at cell i and C_p is the theoretical concentration after complete mixing [Gaudet and Roy, 1995]. If C_N and C_W are the tracer concentrations in the N-River and W-River, respectively, upstream of the confluence, C_p is calculated as follows:

$$C_p = \frac{C_N Q_N + C_W Q_W}{Q_N + Q_W} \tag{2}$$

For $Q_W = 730 \text{ m}^3 \text{ s}^{-1}$, $Q_N = 96 \text{ m}^3 \text{ s}^{-1}$, $C_W = 100 \text{ ppm}$, and $C_N = 0 \text{ ppm}$, for example, as used in the T runs, C_p is of $\sim 88.4 \text{ ppm}$. For the M-simulations and m-simulations C_p is 60.5 and 39.5 ppm, respectively. The mixing layer was defined as the set of cells where the tracer concentration equals $C_p \pm 10\%$, i.e., $\delta(i) = \pm 10\%$. To evaluate the level of mixing at any given cross section, Gaudet and Roy [1995] proposed to calculate δ for the cells with maximum and minimum tracer concentrations in that cross section, δ_{\max} and δ_{\min} . Note that δ_{\max} will be positive, but δ_{\min} will take negative values. Their absolute values will tend to decrease as tracer concentrations get closer to C_p , as a result of mixing. Complete mixing between the side discharge and main stem inflows would be achieved if δ_{\max} and δ_{\min} are in the range $\pm 10\%$ [Gaudet and Roy, 1995].

The second approach to quantify mixing levels consists of calculating the standard deviation of the concentration field in a given cross section σ . Standard deviations will tend to decrease downstream as a result of mixing, and they will become zero when tracer concentrations are uniform in a given cross section. Longitudinal variations of δ_{\min} and σ can be used to assess mixing rates. Note that both approaches to evaluate mixing levels are complementary. Values of δ_{\min} or δ_{\max} remaining equal to those calculated with the initial concentration of the rivers, in particular, are indicative of part of the river flows remaining unmixed in a given cross section. Standard deviation σ , in turn, allows one to determine the level of mixing, even if part of the source water remains unmixed. Note also that both the initial values of δ and σ will depend on flow rates and initial tracer concentrations.

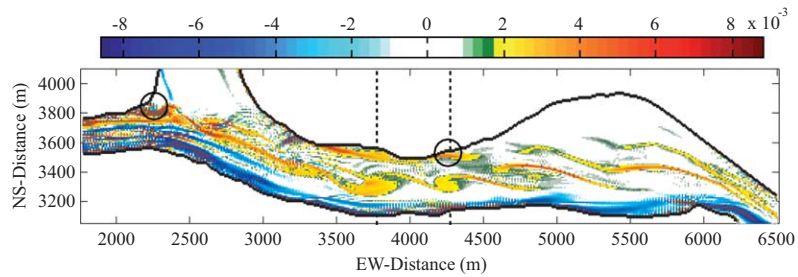


Figure 3. Vertical vorticity (s^{-1}) at the surface plane at 11:30 h. Circles show the locations where eddies are shed (stagnation area and upstream corner of the dead zone). Dashed lines show the location of two eddies shed from the stagnation area, which are ~ 0.5 h apart. Run case *base* in Table 1.

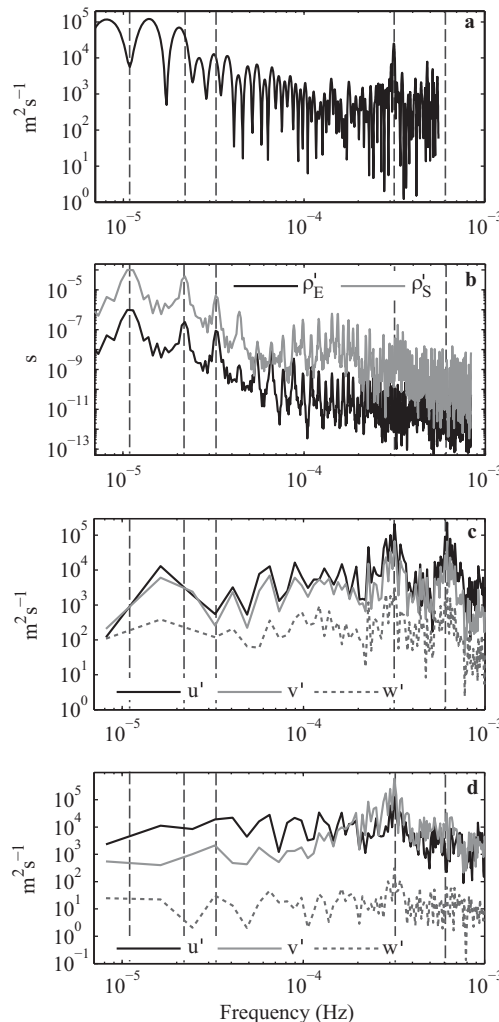


Figure 4. Power spectra of (a) the maximum outward velocities in section B13 ($x_c = 4.7$), (b) the fluctuations of the normalized inflow densities ($(\rho - \rho_0)/\rho_0$) for the Ebro and Segre rivers after a 6 day simulation, and (c and d) the fluctuations of the depth-averaged velocity fields u' , v' , and w' during the last 2 days of simulations at locations (c) A (inside the stagnation zone) and (d) B (mixing layer) shown in Figure 2a. Vertical dashed gray lines show the location of frequencies $f = 1.1 \times 10^{-5}$ Hz, $f = 2.2 \times 10^{-5}$ Hz, $f = 3.3 \times 10^{-5}$ Hz, $f = 3.3 \times 10^{-4}$ Hz, and $f = 6.2 \times 10^{-4}$ Hz. Run case *base* in Table 1.

4. Results and Discussion

4.1. Spatial Distribution of Source Water Near the Confluence

Flow stagnation near the junction apex, flow deflection where each stream enters the confluence, and a shear and mixing layers between the two confluent streams can be identified in the simulations (Figures 2 and 3). This is consistent with the classical model of flow at river confluences proposed by *Best* [1987], except for the absence of flow separation downstream of the junction corner. The absence of flow separation is, however, consistent with the field observations [*Ramón et al.*, 2013] and has also been reported in other studies of natural confluences [e.g., *Biron et al.*, 1993; *Rhoads and Kenworthy*, 1995]. Our simulations are also consistent with those of *Bradbrook et al.* [2000] for asymmetrical confluences, in that water superelevations moved gradually, within the confluence region, toward the bank opposite to the side inflow (Figure 2a). The mixing layer between the confluent streams remains slightly slanted as widens downstream of the confluence (Figure 2). The level of tilting of the mixing interface, though, changes depending on the time of the day (Figures 2e and 2g). These changes are linked to variations in the magnitude of the cross flows (Figures 2f and 2h), which, in turn, are driven either by (1) the development of turbulent eddies shed from the stagnation area (which can be observed from tracer concentrations in Figures 2b–2d and vertical vorticity in Figure 3) and (2) the time-varying density contrast $\Delta\rho/\rho_0$ between streams, which creates large-scale lateral circulation. Each of these processes has different characteristic frequencies (Figure 4); hence, their effect on the velocity and water properties can be isolated. The spectrum of the inflow densities peaked near a frequency of 1.1×10^{-5} Hz (period $T \sim 24$ h), with additional peaks at

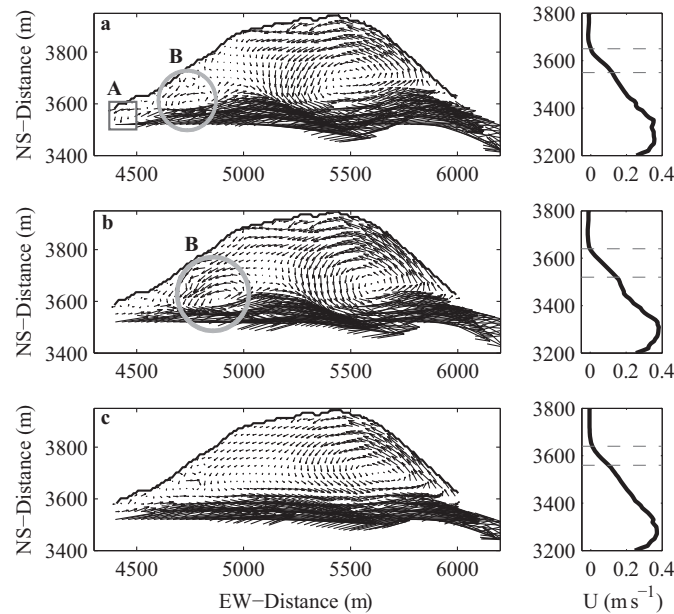


Figure 5. Depth-averaged velocity fields at the dead zone region and depth-averaged downstream velocities U at section B23 ($x_c = 7.2$) located at EW-distance 4960 m. (a) Instant velocities at time $t = 11:30$ h, (b) instant velocities at $t = 12:00$ h, and (c) time-averaged values. Run case *base* in Table 1. The upstream junction corner where eddies are shed (square, A), the evolution of one eddy (circle, B), and the limits of the shear layer between the dead zone and the mainstream (gray dashed lines) are also shown.

$T = 12.7$ h and $T = 8.5$ h corresponding to peaks in the incident radiation signal collected in the meteorological station (Figure 4b). The spectra of the velocity fluctuations in the streamwise (u') and lateral (v') directions within the stagnation area and the mixing interface, however, exhibit peaks at frequencies f_p of 6.2×10^{-4} Hz and 3.2×10^{-4} Hz (Figures 4c and 4d), the former f_p being indicative of vortex shedding from the stagnation area with a period $T = 0.45$ h.

The 6.2×10^{-4} Hz frequency in the stagnation area agrees with the theoretical estimates of frequency of Kelvin-Helmholtz instabilities in shallow mixing layers [Vowinckel *et al.*, 2007] ($f_p = 4.57 \times 10^{-4}$ Hz), calculated as [Sukhodolov and Sukhodolova, 2007]

$$f_p = \frac{U_c}{\gamma} \left[\frac{2 U_c}{Cd \Delta U} \right]^{-1/3} \quad (3)$$

Here $\bar{U}_c (= 0.25 \text{ m s}^{-1})$ is the depth-averaged mixing layer centerline velocity, $\Delta \bar{U} (= 0.331 \text{ m s}^{-1})$ is the difference between the depth-averaged downstream velocities in the W-River and the N-River, and γ (~ 60 m) is the width of the area of flow stagnation (Figure 2a). Hence, the vortices simulated in the shear layer between the W-River and N-River are Kelvin-Helmholtz (KH) structures (Figure 3), consistently with the simulations of the confluence between the Kaskaskia and Copper Slough by Constantinescu *et al.* [2011, 2012], where KH vortices were shown to develop within the shear layer both for $R_M \gg 1$ and $R_M \ll 1$.

4.2. Dead Zone Dynamics

The channel widens in reach R2 (Figure 1) between $x_c = 5.7$ and $x_c = 9.7$ creating a dead zone on the left bank. Instantaneous and mean (averaged over 24 h) depth-averaged flow fields at the dead zone are shown in Figure 5. Note a shear layer develops between the mainstream and the dead zone, with vortices that grow in size and entrain water from the main channel as they move downstream from the upstream corner (Figures 3, 5a, and 5b). Consistently with the simulations of shallow mixing layers around dead zones [Constantinescu *et al.*, 2009], the vortices shown in Figure 5 are KH instabilities. They are shed with a frequency f_p of 3.06×10^{-4} Hz ($T = 0.91$ h), which agrees with the theoretical KH instability frequency ($f_p = 2.7 \times 10^{-4}$ Hz) calculated with equation (3), for $\bar{U}_c = 0.18 \text{ m s}^{-1}$, differences between the depth-averaged downstream velocities in the mainstream and dead zone $\Delta \bar{U} = 0.38 \text{ m s}^{-1}$, and $\gamma \sim 100$ m (Figure 5).

The time-averaged velocity fields reveal the existence of a large gyre within the embayment (Figure 5c). Previous laboratory experiments, though, suggest that a secondary gyre, with the opposite circulation to the primary gyre, should also develop for dead zones having width-to-length ratios $b_0/L_0 < 0.5$ [e.g., Weitbrecht and Jirka, 2001], as is the case of our study site. The fact that this secondary gyre is not reproduced in our simulations may be the result of the semicircular planform geometry of the embayment (see Figure 1) or bathymetric effects. As suggested by Sukhodolov *et al.* [2002], the riverbed geometry of dead zones with complex morphological structures in natural rivers may produce velocity patterns that differ from those observed in laboratory studies. For example, they observed a secondary gyre that rotates in the same direction as the main gyre. Muto *et al.* [2002]

Table 2. Time-Averaged and Section-Averaged Magnitude ($m s^{-2}$) of Terms in Equation (4) (Transverse Momentum Equation) at $x_c = 4.7$ and $x_c = 15.3^a$

Term in Equation (4)	Section B13 ($x_c = 4.7$)			Section B49 ($x_c = 15.3$)		
	Run Case			Run Case		
	T1	T5	T8	T1	T5	T8
2 ^b	-2.1×10^{-5}	-1.7×10^{-5}	-1.8×10^{-5}	2.9×10^{-6}	4.3×10^{-6}	2.3×10^{-6}
3 ^c	3.8×10^{-5}	3.8×10^{-5}	3.7×10^{-5}	-3.4×10^{-5}	-3.4×10^{-5}	-4.3×10^{-5}
4 ^d	-1.1×10^{-5}	-1.1×10^{-5}	-3.4×10^{-5}	2.8×10^{-5}	3.5×10^{-5}	4.7×10^{-5}
5 ^e	4.9×10^{-6}	-7.8×10^{-9}	-2.1×10^{-5}	-3.5×10^{-6}	8.9×10^{-9}	7.2×10^{-6}
6 ^f	3.2×10^{-6}	6.2×10^{-7}	-1.7×10^{-6}	-6.1×10^{-7}	-2.2×10^{-7}	2.0×10^{-6}

^aNegative values indicate forcing toward the left bank.

^bAdvection.

^cCentrifugal forcing.

^dBarotropic forcing.

^eBaroclinic forcing.

^fTurbulent diffusion.

also observed a unique small cell in an embayment in a natural river ($b_0/L_0 = 0.25$), which they attributed to bed irregularities, such as bed undulation. Alternatively, the absence of this secondary gyre in our simulations could be due to the inability of the two-equation turbulence model closure. *Gualtieri* [2008], for example, also failed to reproduce the secondary gyre in his 2-D computations of the experiment of *Weitbrecht and Jirka* [2001] with a standard two-equation $k-\epsilon$ turbulence model. Later, *Gualtieri et al.* [2009] were able to reproduce the laboratory experiments of *Muto et al.* [2000] on a flume with a unique dead zone. They compared the standard $k-\epsilon$ model, which assumes isotropic turbulence, and a nonisotropic Reynolds stress model, and found that the estimates of the transverse velocities, though similar, were better predicted when the anisotropy of the Reynolds stresses was explicitly represented.

4.3. Physical Drivers of Cross-Stream Fluid Motion

The contribution of baroclinic forces, associated with the time-varying side-inflow density, to the development of lateral circulation and, thus, mixing layer distortion, is examined next. Following assumptions by *Kalkwijk and Booij* [1986], adding the lateral baroclinic forces and neglecting Coriolis, the transverse momentum equation can be written as

$$\underbrace{\frac{\partial v}{\partial t}}_{(1)} + u \underbrace{\frac{\partial v}{\partial x}}_{(2)} - \underbrace{\frac{u^2}{R_s}}_{(3)} + \left(\underbrace{g \frac{\partial \zeta}{\partial y}}_{(4)} + \underbrace{g \frac{1}{\rho_0} \int_z^\zeta \frac{\partial \rho}{\partial y} dz'}_{(5)} \right) - \underbrace{\frac{\partial}{\partial z} \left(A_z \frac{\partial v}{\partial z} \right)}_{(6)} = 0 \quad (4)$$

Here u and v represent the velocity components in the streamwise x direction and lateral y direction; g is the acceleration of gravity; ζ is the free surface elevation; and A_z is the kinematic eddy viscosity in the vertical z direction. The first and second terms in equation (4) are local acceleration and lateral inertia; terms 3 through 5 represent the centrifugal F_c , barotropic F_p , and baroclinic F_b forcings of the cross flow. The sixth term represents momentum transport by turbulent diffusion. Note that R_s in term 3 is negative for channels veering to the left and positive otherwise. Negative values in equation (4) indicate acceleration toward the left bank.

The time-averaged magnitude of each term in equation (4) was evaluated from simulated variables at $x_c = 4.7$ and $x_c = 15.3$, in three different scenarios with $\Delta\rho/\rho_0$ set to 0 and $\pm 2.4 \times 10^{-4}$ (runs T1, T5, and T8 in Table 1). The results are shown in Table 2. For neutrally buoyant side inflows (run T5), the cross-stream motion is largely controlled by a balance between F_c and F_p , both of $O(10^{-5}) m s^{-2}$. For nonneutrally buoyant side inflows (runs T1, T8), in turn, even with weak density differences, the force balance becomes even more complex, and F_b becomes one of the dominant terms, also of $O(10^{-5}) m s^{-2}$, especially immediately downstream of the confluence where the density contrast is larger. The magnitude of F_c compared to that

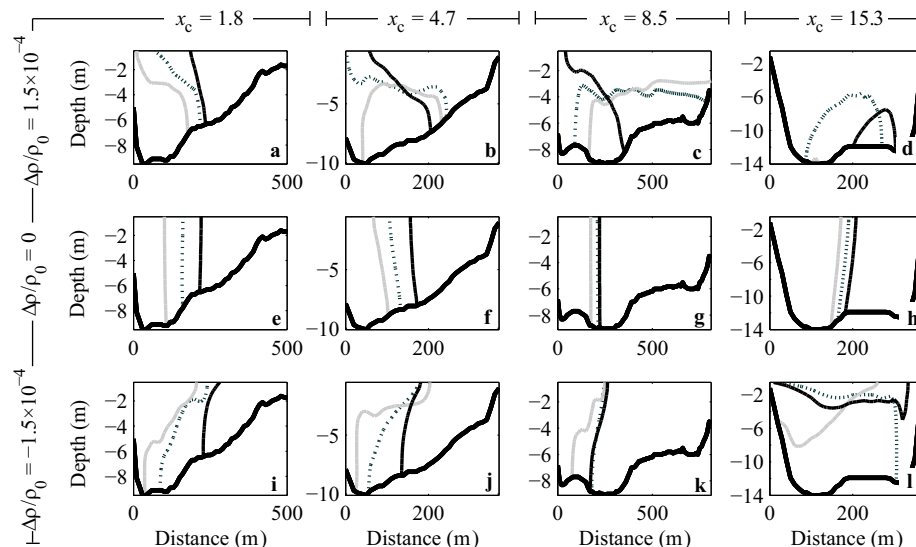


Figure 6. Time-averaged location of isolines of tracer concentration $C = C_p$ for different discharge ratios R_q and density contrasts $\Delta\rho/\rho_0$ between the Ebro and Segre rivers and distance downstream. Sections (a, e, and i) B2 ($x_c = 1.8$), (b, f, and j) B13 ($x_c = 4.7$), (e, g, and k) B28 ($x_c = 8.5$), and (d, h, and l) B49 ($x_c = 15.3$). $R_q = 0.13$ (black solid lines), $R_q = 0.65$ (black dotted lines), and $R_q = 1.53$ (gray solid lines).

of F_b will vary depending on the cross section. The former can be quantified using the maximum lateral velocities in a curved channel v_c estimated as in *Johannesson and Parker* [1988], $v_c = 6UD/R_s$. The ideal speed of the gravity current in the absence of shear and mixing, $c = (g \Delta\rho/\rho_0 D)^{0.5}/2$ will be taken as a proxy of the magnitude of F_b . This value increases from 0.03 m s^{-1} for $\Delta\rho/\rho_0 = \pm 3.2 \times 10^{-5}$ to 0.07 m s^{-1} for $\Delta\rho/\rho_0 = \pm 2.4 \times 10^{-4}$. Lateral velocities induced by F_c are weak compared to those induced by F_b especially in the first bend, where, for $U = 0.32 \text{ m s}^{-1}$ and $D = 10 \text{ m}$ as observed at $x_c = 4.7$, $v_c \sim 6.4 \times 10^{-3} \text{ m s}^{-1}$. Modeled maximum outward lateral velocities in this section agree with these estimates. For example, low-pass filtered ($f < 4 \times 10^{-5} \text{ Hz}$) cross-flow velocities near surface at $x_c = 4.7$ ranged from 3.2 to 5.1 cm s^{-1} depending on $\Delta\rho/\rho_0$. This indicates that lateral motion is largely set up by the existence of density contrasts. Farther downstream, at $x_c = 15.3$ ($U = 0.2 \text{ m s}^{-1}$, $D = 14 \text{ m}$), v_c increases to ca. 0.013 m s^{-1} , and the centrifugal and baroclinic forcings become comparable.

Baroclinic and centrifugal forcings act in the same or in opposite direction, depending on whether side inflows are positively or negatively buoyant and on whether the flow bends to the left or to the right. For example, in the first bend to the left (reach R1), the cross-stream flow will be stronger in response to increases in density contrasts for $\Delta\rho/\rho_0 > 0$, tilting and distorting the mixing layer toward the right bank (Figures 6a and 6b). For $\Delta\rho/\rho_0 = 0$, F_c is weak to effectively tilt the mixing layer (Figures 6e and 6f). For $\Delta\rho/\rho_0 < 0$, the mixing interface remains largely vertical until density contrasts are large enough to overcome F_c ($|\Delta\rho/\rho_0| > O(10^{-6})$) and to tilt the mixing interface toward the left bank (Figures 6i and 6j). In the second bend to the right ($x_c \geq 10.3$, reach R3), negatively buoyant side inflows increase cross-flow strength, and the mixing interface tilts to the left (Figures 6d, 6h, and 6l).

Lateral inertia (term 2) is particularly significant close to the confluence (see section B13 in Table 2). Its magnitude is, in turn, linked to the momentum ratio R_M . As a result of changes in R_M , several changes occur in the flow field near the confluence. First, as R_M increases, the location of the mixing layer moves farther away from the tributary bank (see, for example, Figures 6e and 6f). This is consistent with earlier work conducted under nearly neutrally buoyant conditions in river confluences [e.g., *Biron et al.*, 1993; *Rhoads and Kenworthy*, 1995, 1998]. Second, under nonneutrally buoyant conditions, the tilting of the mixing layer increases (Figures 6a and 6i).

4.4. Mixing Rates Between the Ebro and Segre Rivers

In the *base case* simulation, mixing is complete at the most downstream section, almost 7.5 km ($x_c \sim 18.7$) from the junction apex, where average absolute values of δ_{\min} and δ_{\max} become $< 10\%$ (Figure 7a). Minimum deviation δ_{\min} remained constant and close to -100% (i.e., indicative of weak mixing) but only for

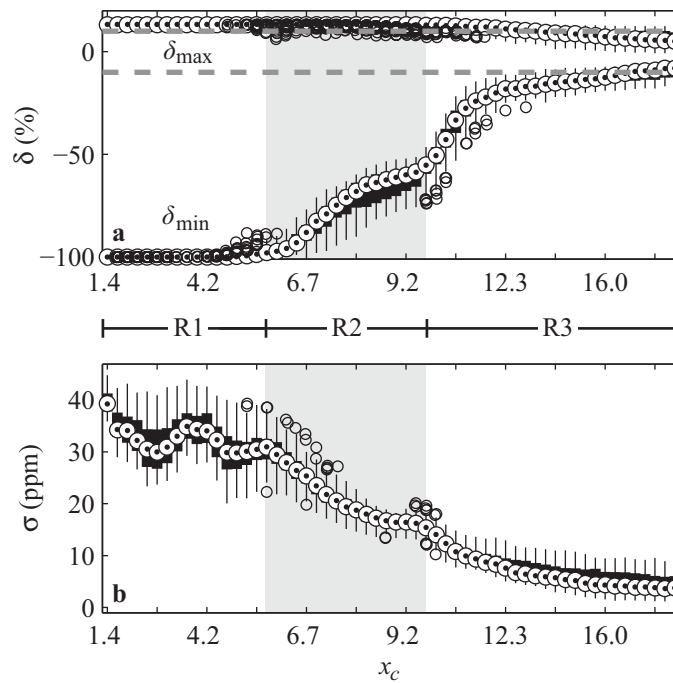


Figure 7. Boxplot of (a) maximum δ_{\max} and minimum δ_{\min} deviations from complete mixing δ (%) and of (b) standard deviations σ (ppm) of tracer concentrations in sections B1–B58 for the base case simulation in Table 1. The gray dashed lines in Figure 7a show the upper and lower limits ($\delta_{\max} = 10\%$ and $\delta_{\min} = -10\%$) within which complete mixing is achieved [Gaudet and Roy, 1995]. The shaded area shows sections within reach R2.

ures 7a and 7b. These changes can only be attributed in our simulations to either changes in inflow densities (Figure 4b) or the existence of large coherent structures developing at the dead zone (Figure 5) and at the stagnation area (Figures 2, 3, and 4c). The time series of σ and $\Delta\rho/\rho_0$ at $x_c = 4.7$, $x_c = 8.5$, and $x_c = 15.3$ during the last two days of simulation are shown in Figures 8a–8c. The spectra of the signals are also shown (Figures 8d–8f). Note that the variability of σ in reach R1, with peak frequencies near 3.1×10^{-4} Hz (Figure 8d), is largely associated with unsteady large coherent structures which exhibit similar frequencies (see Figures 4c and 4d). The contribution of the coherent structures, however, weakens downstream (for example, at $x_c = 15.3$) where the variability of σ (from 2 ppm to 9 ppm) becomes dominated by the diurnal changes in inflow densities (Figure 8f).

$x_c \leq 5.4$ within reach R1. Strong mixing occurs, as revealed by increasing values of δ_{\min} (or decreasing σ , Figure 7 and Table 3) once in reach R2, where the channel widens to form a dead zone ($5.7 \leq x_c \leq 9.7$), and downstream, as the channel narrows again and bends to the right ($x_c > 9.7$, reach R3). Mixing lengths between the W-River and N-River are of $O(10^1)$ channel widths which are indicative of rapid mixing between the confluent streams, consistently with the field observations of Ram3n et al. [2013] and the prior results on mixing in river confluences [e.g., Rhoads and Kenworthy, 1995; Rhoads and Sukhodolov, 2001; Lane et al., 2008, and references therein].

Mixing rates, as revealed by δ_{\min} and σ , were also subject to changes in time, as shown by the upper and lower whiskers in Fig-

Table 3. Time-Averaged Mixing Rates (Absolute Values)— $\Delta\sigma/\Delta x$ (ppm m^{-1})—Evaluated in Reaches R1, R2, R3, and Along the Study Reach (Total)

Run Case	R1	R2	R3	Total
Base	5.3×10^{-3}	9.8×10^{-3}	2.4×10^{-3}	5.1×10^{-3}
T1	1.1×10^{-2}	6.2×10^{-3}	1.9×10^{-3}	5.3×10^{-3}
T2	9.1×10^{-3}	7.9×10^{-3}	2.5×10^{-3}	5.6×10^{-3}
T3	4.7×10^{-3}	1.0×10^{-2}	2.2×10^{-3}	5.0×10^{-3}
T4	3.7×10^{-3}	9.2×10^{-3}	2.0×10^{-3}	4.4×10^{-3}
T5	3.7×10^{-3}	3.7×10^{-3}	3.8×10^{-3}	4.0×10^{-3}
T6	5.0×10^{-3}	7.4×10^{-3}	4.1×10^{-3}	5.3×10^{-3}
T7	7.1×10^{-3}	7.6×10^{-3}	2.7×10^{-3}	5.2×10^{-3}
T8	8.7×10^{-3}	7.2×10^{-3}	1.9×10^{-3}	5.1×10^{-3}
M1	5.5×10^{-3}	2.3×10^{-3}	5.5×10^{-3}	4.8×10^{-3}
M2	3.7×10^{-3}	1.7×10^{-3}	8.0×10^{-3}	5.4×10^{-3}
M3	2.9×10^{-3}	1.5×10^{-3}	3.6×10^{-3}	2.9×10^{-3}
M4	4.9×10^{-3}	1.2×10^{-2}	4.0×10^{-3}	6.3×10^{-3}
M5	5.7×10^{-3}	8.7×10^{-3}	4.6×10^{-3}	5.8×10^{-3}
m1	1.1×10^{-2}	3.1×10^{-3}	3.8×10^{-3}	5.5×10^{-3}
m2	8.4×10^{-3}	2.0×10^{-3}	5.5×10^{-3}	5.1×10^{-3}
m3	8.0×10^{-3}	1.5×10^{-3}	2.6×10^{-3}	3.4×10^{-3}
m4	1.0×10^{-2}	8.6×10^{-3}	2.5×10^{-3}	6.2×10^{-3}
m5	9.0×10^{-3}	5.7×10^{-3}	4.3×10^{-3}	5.8×10^{-3}

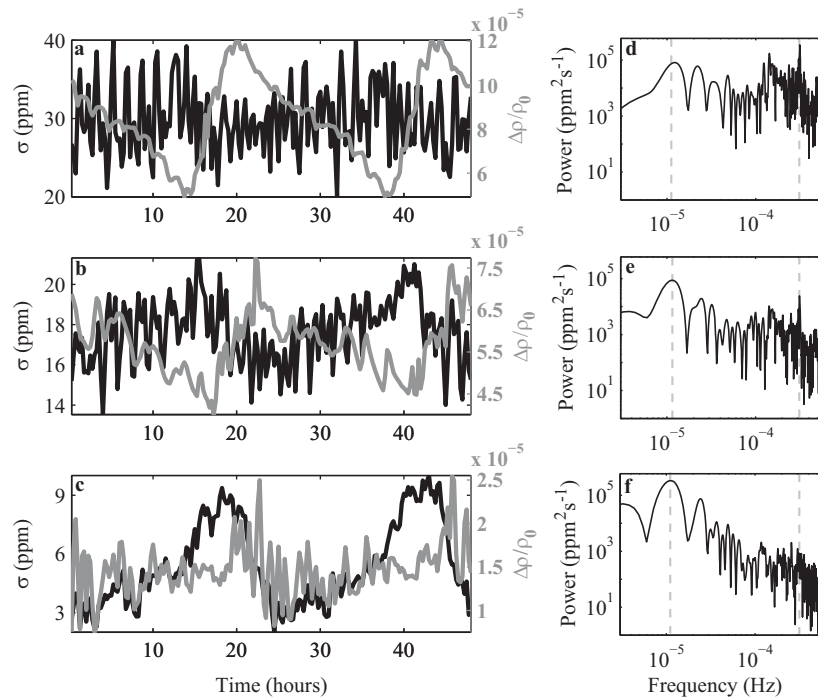


Figure 8. (a–c) Time-varying standard deviation σ of tracer concentrations (black lines) and density contrast $\Delta\rho/\rho_0$ between rivers (gray lines) during the last 2 days of simulations in the *base case* simulation (Table 1). (d–f) Spectral curves for the time-varying σ . (Figures 8a and 8d) Section B13 ($x_c = 4.7$) in reach R1, (Figure 8b and 8e) section B28 ($x_c = 8.5$) in reach R2, and (Figure 8c and 8f) section B49 ($x_c = 15.3$) in reach R3. The frequency peaks $f_p = 1.14 \times 10^{-5}$ Hz (period $T \sim 24$ h) and $f_o = 3.1 \times 10^{-4}$ Hz ($T = 0.9$ h) characteristic of the density signal and of the coherent structures, respectively, are shown (gray dashed lines).

4.5. Influence of Density Differences on Mixing Rates

Time-averaged values of σ for runs T1–T8 (Table 1) are plotted in Figure 9a as function of the distance downstream of the junction apex x_c and the density contrast $\Delta\rho/\rho_0$. For any given run with a fixed value of $\Delta\rho/\rho_0$, the separation between isolines will vary with distance and represents the magnitude of the local mixing

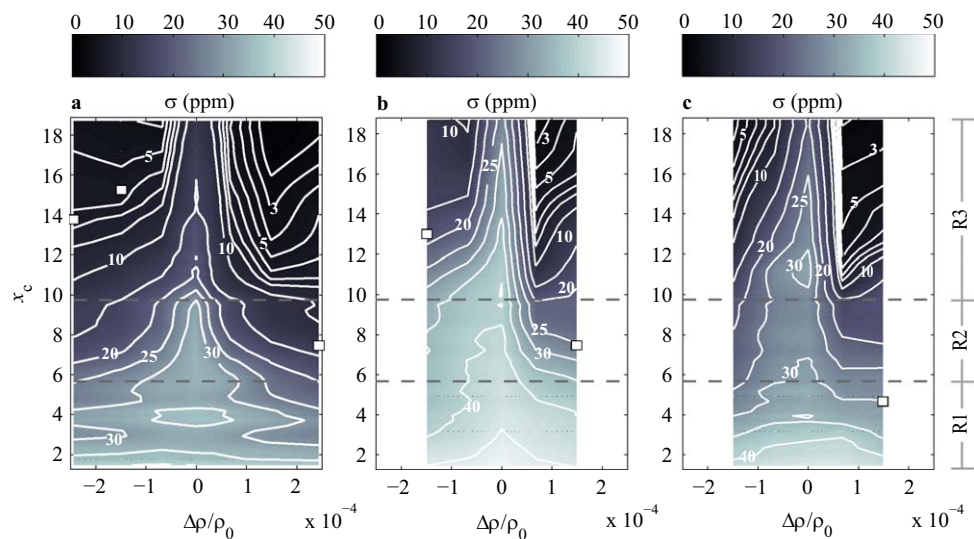


Figure 9. Variation with nondimensional distance downstream of the junction apex (x_c) of the linearly interpolated time-averaged values of standard deviations σ , for different density contrasts ($\Delta\rho/\rho_0$) between the Ebro and Segre rivers. Run cases (a) T1–T8, (b) M1–M5, and (c) m1–m5 in Table 1. The location of $x_c = 5.7$ —start of reach R2—and $x_c = 9.7$ —start of reach R3—is shown (gray dashed lines). Note that the resolution of the σ isolines (white lines) increases downstream from gradients 5 ppm within reaches R1 and R2 to gradients of 1 ppm within reach R3. White squares in Figures 9b–9d show locations of x_H points.

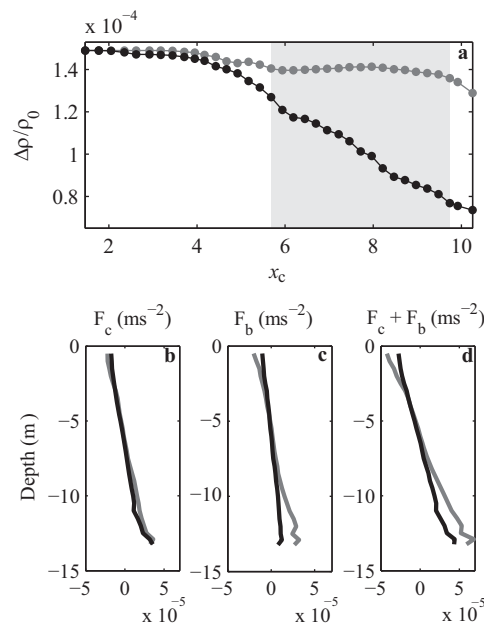


Figure 10. (a) Variation with distance downstream of the time-averaged density contrast between the Ebro and Segre rivers, and time-averaged and width-averaged (b) centrifugal forcing F_c , (c) baroclinic forcing F_b , and (d) $F_c + F_b$ in section B35 ($x_c = 10.3$) for runs M5 (gray line) and m5 (black line). The shaded area in Figure 10a shows sections within reach R2.

rate: the closer the isolines the stronger the mixing. Values of mixing rates $\Delta\sigma/\Delta x$, evaluated in reaches R1–R3 and along the study reach ($x_c = 0$ –18.7), are also shown in Table 3. Mixing rates, for example, tend to be larger in reach R2 compared to reach R1, consistently with Figure 7. The weakest mixing ($\Delta\sigma/\Delta x = 4.0 \times 10^{-3}$ ppm m^{-1}) occurred for $\Delta\rho/\rho_0 = 0$, tending to increase for weakly buoyant side inflows in response to changes of $O(10^{-5})$ in $\Delta\rho/\rho_0$. For the largest values of $\Delta\rho/\rho_0$ tested ($>10^{-4}$), in turn, mixing rates in the study reach tended to decrease in response to increases in side-inflow buoyancy. Note that the differences in mixing rates between weakly and strongly buoyant side inflows occur mainly in reach R3. In this reach, mixing rates appeared to be weaker for strongly buoyant conditions (more spaced isolines in Figure 9a and Table 3) and stronger for weakly buoyant conditions. For positively buoyant inflows maximal mixing rates occurred at $\Delta\rho/\rho_0 = 1.5 \times 10^{-4}$ ($\Delta\sigma/\Delta x = 5.6 \times 10^{-3}$ ppm m^{-1}). For negatively buoyant inflows, maximal rates occurred at $\Delta\rho/\rho_0 = -6.8 \times 10^{-5}$ ($\Delta\sigma/\Delta x = 5.3 \times 10^{-3}$ ppm m^{-1}). These mixing rates, in general, were up to 40% larger than those simulated with $\Delta\rho/\rho_0 = 0$ (Table 3).

Any differences in mixing rates between simulations in Figure 9a should be the result of differences in (1)

the contact area between the water masses, where the spatial gradients of tracer concentration are significant, and/or (2) the diffusion coefficients near that mixing interface. The contact area at any given cross section was identified as the set of vertical and horizontal interfaces between adjacent cells where the tracer concentration changes from $C > C_p$ to $C < C_p$. It can be decomposed in the model into a set of interfaces available for vertical mixing, of area S_v , and another set of interfaces available for horizontal mixing, of area S_h . Surface of contact areas (S_v and S_h) and their average vertical diffusion coefficients at several cross sections downstream of the confluence are shown in Table 4, for side inflows with different density contrasts.

Table 4. Time-Averaged Mean Values at the Mixing Interface Between the Ebro and Segre Rivers at $x_c = 1.8, x_c = 4.7, x_c = 8.5,$ and $x_c = 15.3^a$

$\Delta\rho/\rho_0$	Section B2, $x_c = 1.8$			Section B13, $x_c = 4.7$		
	K_z ($m^2 s^{-1}$)	S_h (m^2)	S_v (m^2)	K_z ($m^2 s^{-1}$)	S_h (m^2)	S_v (m^2)
2.4×10^{-4}	6.31×10^{-3}	55.10	833.23	2.78×10^{-3}	64.75	2075.78
1.5×10^{-4}	8.02×10^{-3}	58.51	492.81	3.87×10^{-3}	68.92	1479.28
6.8×10^{-5}	9.16×10^{-3}	60.00	86.82	5.05×10^{-3}	73.52	825.40
3.2×10^{-5}	8.52×10^{-3}	60.00	37.12	6.14×10^{-3}	73.13	702.97
0	9.00×10^{-3}	60.00	51.19	6.49×10^{-3}	74.81	157.64
-6.8×10^{-5}	6.54×10^{-3}	59.00	175.23	6.47×10^{-3}	76.00	239.22
-1.5×10^{-4}	6.79×10^{-3}	59.21	548.33	6.94×10^{-3}	79.00	457.13
-2.4×10^{-4}	4.35×10^{-3}	59.73	1015.82	5.52×10^{-3}	82.21	863.33
		Section B28, $x_c = 8.5$			Section B49, $x_c = 15.3$	
2.4×10^{-4}	1.77×10^{-3}	60.93	3522.83	6.02×10^{-3}	116.07	2352.27
1.5×10^{-4}	2.37×10^{-3}	77.68	3103.30	5.45×10^{-3}	49.38	1029.28
6.8×10^{-5}	4.11×10^{-3}	84.99	1355.30	7.73×10^{-3}	132.38	550.67
3.2×10^{-5}	5.79×10^{-3}	85.00	630.85	8.08×10^{-3}	123.89	211.08
0	8.07×10^{-3}	84.27	18.94	1.04×10^{-2}	114.78	259.45
-6.8×10^{-5}	6.94×10^{-3}	85.00	430.22	2.16×10^{-3}	106.17	2278.04
-1.5×10^{-4}	5.08×10^{-3}	83.01	926.85	2.32×10^{-3}	44.79	3248.66
-2.4×10^{-4}	3.11×10^{-3}	73.92	1663.57	2.50×10^{-3}	120.01	2929.74

^aRuns T1–T8 in Table 1.

4.5.1. Mixing Layer Distortion

As shown in Figure 6, the tilting of the mixing interface, and hence the contact area between the rivers, is tightly linked to the magnitude of $\Delta\rho/\rho_0$. The changes in S_h occurring in response to buoyant side inflows are, in general, weak (at most of $\pm 10\%$) within reach R1 compared to the changes in the area available for vertical mixing S_z (Table 4). For example, the area S_z was ca. 13 and 5 times larger for $\Delta\rho/\rho_0 = +2.4 \times 10^{-4}$ and $\Delta\rho/\rho_0 = -2.4 \times 10^{-4}$, respectively, than for $\Delta\rho/\rho_0 = 0$, at $x_c = 4.7$ (compare, also, Figures 6b, 6f, and 6j). Farther downstream, at $x_c = 8.5$, S_z for $\Delta\rho/\rho_0 = \pm 2.4 \times 10^{-4}$ is 2 order of magnitude larger than S_z for $\Delta\rho/\rho_0 = 0$ (Table 4 and Figures 6c, 6g, and 6k). Note, also in Table 4, that S_z tends to be larger for positively buoyant side inflows, compared to the cases of negatively buoyant side inflows at $x_c = 4.7$. This occurs also at $x_c = 8.5$ and can be first attributed to the effect of bottom friction, which will tend to decelerate the downslope lateral flow of negatively buoyant side inflows, but will not affect the lateral near-surface motion of positively buoyant side inflows. Second, it can also be understood as a result of the interplay between F_c and F_b (equation (4)). Although the cross flows, v_c , induced by F_c are small compared to those induced by F_b , c , in reaches R1 and R2 (see section 4.3), they can delay the tilting of the mixing interface for $\Delta\rho/\rho_0 < 0$. For example, for $U = 0.32 \text{ m s}^{-1}$, $v_c \sim 6.4 \times 10^{-3} \text{ m s}^{-1}$, and $c \sim \pm 0.07 \text{ m s}^{-1}$, as expected for $\Delta\rho/\rho_0 = \pm 2.4 \times 10^{-4}$ (see section 4.3), S_z could increase ca. 500 m^2 more for positively buoyant side inflows in the time the mean flow goes from $x_c = 1.8$ to $x_c = 4.7$.

4.5.2. Eddy Diffusivities

As density contrasts increase and the mixing layer tilts, the vertical density gradients across the mixing interface tend to suppress turbulent motions, causing vertical diffusivities K_z to decrease. These effects of side-inflow buoyancy on K_z , though, are smaller than the effects on the area of contact near the confluence. For example, at $x_c = 1.8$, K_z averages $\sim 0.01 \text{ m}^2 \text{ s}^{-1}$ at the interface for $\Delta\rho/\rho_0 = 0$ (Table 4), but is 1.5 times lower for $\Delta\rho/\rho_0 = +2.4 \times 10^{-4}$ (Table 4). By contrast, the interface area is up to 16 times larger under non-neutrally buoyant conditions, compared to the simulation with $\Delta\rho/\rho_0 = 0$. These results, hence, suggest that the higher mixing rates under nonneutrally buoyant conditions are largely the result of a higher level of distortion of the mixing layer. This conclusion is consistent with simulations [Bradbrook *et al.*, 2001; Biron and Lane, 2008] and field observations [Rhoads and Kenworthy, 1995; Rhoads and Sukhodolov, 2001] of river confluences reported earlier. The mechanisms causing distortion in Ribarroja, though, are not the same as those reported earlier.

Once the side inflows have reached the opposite side of the main channel and the interface becomes nearly horizontal, further changes in the density contrast do not affect the contact area. Note, for example, that S_z is nearly constant for $\Delta\rho/\rho_0 > +1.5 \times 10^{-4}$, at $x_c = 8.5$ (Table 4). The effects of side-inflow buoyancy on K_z , though, become important at that point. At $x_c = 8.5$, in particular, K_z for $\Delta\rho/\rho_0 = +1.5 \times 10^{-4}$ is 1.3 times higher than K_z for $\Delta\rho/\rho_0 = +2.4 \times 10^{-4}$ (Table 4). The distance downstream to this point where the interface becomes horizontal will be referred to as x_H and has been plotted in Figure 9a for those simulations where the mixing interface became horizontal within the computational domain. Note that mixing rates decrease (i.e., the spacing between isolines increases) downstream of x_H in Figure 9a. Any changes in the contact area occurring downstream of x_H will be the result of the balance between centrifugal forcing, controlled by channel geometry, and the stability of the water column, resulting from vertical density gradients. Inflows with larger density contrasts will lead to more stable interfaces downstream, which will tend to remain closer to horizontal in channels with a given curvature. At $x_c = 15.3$, for example, S_z for $\Delta\rho/\rho_0 = +2.4 \times 10^{-4}$ is almost twice the value calculated for $\Delta\rho/\rho_0 = +1.5 \times 10^{-4}$ (Table 4). Thus, the negative effect of large density contrasts on mixing rates should be understood as a result of the development of very stable horizontal interfaces where mixing is suppressed by vertical density gradients. Centrifugal forcing, in turn, will tend to generate lateral density gradients, hence, increasing mixing rates.

4.5.3. Influence of Momentum Ratios

The lowest mixing rates still occur for $\Delta\rho/\rho_0 = 0$, independently of R_M (or R_q) (Figures 9b and 9c and Table 3). Also independently of R_M , mixing rates increase or decrease in response to increases in $|\Delta\rho/\rho_0|$, depending on whether the side inflows are weakly or strongly buoyant. The value of $\Delta\rho/\rho_0$ for maximal mixing rates ($\Delta\rho/\rho_0^*$), though, changes in response to stronger side-inflow momentum. Note that $\Delta\rho/\rho_0^*$ decreases in response to increases in R_M for positively buoyant side inflows but increases for $\Delta\rho/\rho_0 < 0$. The site where

the mixing interface becomes horizontal also changes in response to changes in R_M . For positively buoyant side flows, x_H moves upstream as a result of stronger side-inflow momentum, but it moves downstream for negatively buoyant side inflows. Note that for $R_q = 1.53$ the interface did not even become horizontal (Figure 6l) for the most negatively buoyant flows tested, and, hence, mixing rates always increased in response to increases in side-inflow density (see Table 3 and the upper left side of the plot in Figure 9c, where the isolines are monotonically decreasing as a function of $\Delta\rho/\rho_0$).

This different behavior of x_H for positively versus negatively buoyant side inflows can be understood as the result of the interplay between the inertia of the tributary and the mixing induced by its initial acceleration at and near the confluence. The inertia of the tributary favors the distortion of the mixing interface both for positively and negatively buoyant side inflows (Figures 6a and 6i) and, as a result, mixing rates increases. Compare, for example, the location of the isoline of 40 ppm in Figures 9b and 9c, for M-simulations and m-simulations in which the initial σ , upstream the confluence, is similar. For $\Delta\rho/\rho_0 > 0$, a horizontal mixing interface develops within reaches R1 or R2 which counteracts the mixing induced by the lateral inertia of the tributary. For $\Delta\rho/\rho_0 < 0$, a horizontal mixing interface does not develop in R1 or R2 and mixing continues increasing. The effect on mixing of the tributary lateral inertia increases with R_M , and, as a result, the density contrast between the two sources of water $\Delta\rho/\rho_0$, and thus F_b , decreases more rapidly downstream with increasing R_M (Figures 10a and 10b). Once in reach R3, the interplay between F_b and F_c (Figures 10b–10d) pushes the mixing interface to tilt toward the left bank for negatively buoyant side inflows. A weaker F_b explains why for $R_q = 1.53$ the interface did not become horizontal within reach R3.

As R_M increases, the influence on mixing of the dynamics of the dead zone decreases. See, for example, that σ remains equal to ca. 30 ppm within reach R2 for $\Delta\rho/\rho_0 = 0$ and $R_M = 4.58$ in Figure 9c. This is the result of the mixing interface between rivers moving laterally toward the bank opposite to the tributary bank (where the dead zone is located) as R_M increases (Figure 6), so that it moves farther away from the shear layer that forms between the mainstream and the dead zone (Figures 3 and 5). The interaction between the mixing interface and the dead zone will be then dependent on the mechanisms forcing the distortion of the mixing layer (here, the baroclinic forcing) which brings them closer again (Figures 6c, 6g, and 6k).

5. Summary and Conclusions

The effect of weak density contrasts on mixing rates between two rivers of asymmetrical confluence and meandering planform were analyzed with a three-dimensional model. Mixing rates under weak density contrast of up to $O(10^{-1}) \text{ kg m}^{-3}$, typical of large river confluences, were up to 40% larger than those simulated under neutrally buoyant conditions. This increase on mixing is largely the result of density contrasts leading to changes in the contact area between water masses available for mixing. Stronger density contrasts, which might lead to nearly horizontal contact areas shortly downstream of the confluence, will lead to weaker mixing rates compared to weakly buoyant conditions, as a result of the stabilizing effect of strong vertical density gradients. As shown through unsteady simulations, even weak time-varying density differences, driven by diurnal changes in inflow temperatures, could lead to significant changes in mixing rates between the confluent rivers depending on the time of the day.

The distortion of the mixing layer is largely controlled by the strength of the cross-stream motions, which, in turn, is driven by a subtle interaction between baroclinic and centrifugal forces. The first is associated with the magnitude and sign of the density contrasts; the second, with the magnitude and sign of the curvature. In our study site, with the channel veering to the left downstream of the confluence, centrifugal forcing increases the distortion of the mixing layer induced by positively buoyant side inflows, but, tends to diminish the tilting of the interface that results from negatively buoyant inflows. Hence, as a result of the channel geometry, mixing rates at river confluences could respond differently depending on whether the side inflows are negatively buoyant or positively buoyant. As the side-inflow inertia increases, the mixing interface moves closer to the bank opposite to the side inflow and mixing increases immediately downstream of the confluence, favoring the development of horizontal mixing layers for weakly density contrasts. These results, in general, strongly suggest that density differences

between confluent rivers, even though weak, have a strong impact on mixing rates and patterns at large river confluences.

Mixing ratios also oscillated in time as a result of large-scale coherent vortices developing (a) in the shear layer between the two river sources near the confluence and (b) in a dead zone sited shortly downstream. The dead zone, though, appears—under the conditions observed in the field—as the site where mixing is more energetic. Changes in standard deviations of 0.01 ppm m^{-1} were found in the dead zone, almost twice the rates observed in other reaches. This suggests that the existence of channel irregularities near confluences leading to the development of dead zones might accelerate the rate at which water masses mix downstream of river junctions. The contribution of side irregularities to mixing, though, will depend on whether the mixing interface between the confluent rivers becomes close or not to the shear layer generated at those sites. This, in turn, will depend on (1) the momentum ratio between the confluent rivers, which determines the position of the vertical mixing interface to the tributary bank, under neutrally buoyant conditions, and (2) the forces controlling the tilting of the interface.

Acknowledgments

This work was part of a collaborative agreement between the University of Barcelona and the University of Granada to work jointly in the Project “Gestión hidráulica y técnicas de detección remota aplicada al control de poblaciones mejillón cebra: el caso del embalse de Ribarroja y el tramo inferior del río Ebro,” funded by the Spanish Ministry of the Environment. The parallel version of the hydrodynamic model was developed under project CGL2008-06101/BOS, funded by the Spanish Ministry of Science and Innovation. We are also in debt with the scientific personnel from ENDESA-Medio Ambiente.

References

- Acosta, M., M. Anguita, F. J. Rueda, and F. J. Fernández-Baldero (2010), Parallel implementation of a semi-implicit 3D lake hydrodynamic model, in Proceedings of the 2010 International Conference on Computational and Mathematical Methods in Science and Engineering, Addlink/COMSOL, Almería, Spain.
- Benda, L., N. L. Poff, D. Miller, T. Dunne, G. Reeves, G. Pess, and M. Pollock (2004), The network dynamics hypothesis: How channel networks structure riverine habitats, *BioScience*, 54(5), 413–427, doi:10.1641/0006-3568(2004)054[0413:TNDHHC]2.0.CO;2.
- Best, J. L. (1987), Flow dynamics at river channel confluences: Implications for sediment transport and bed morphology, in *Recent Developments in Fluvial Sedimentology, Spec. Publ.*, 39, edited by F. G. Ethridge, R. M. Flores, and M. D. Harvey, pp. 27–35, Soc. of Econ. Paleontol. and Mineral., Tulsa, Okla.
- Bigelow, P. E., L. E. Benda, D. J. Miller, and K. M. Burnett (2007), On debris flows, river networks and the spatial structure of channel morphology, *For. Sci.*, 53(2), 220–238.
- Biron, P., B. De Serres, A. G. Roy, and J. L. Best (1993), Shear layer turbulence at an unequal depth channel confluence, in *Turbulence: Perspectives on Flow and Sediment Transport*, edited by N. J. Clifford, J. R. French, and J. Hardisty, pp. 197–193, John Wiley, Chichester, U. K.
- Biron, P. M., and S. N. Lane (2008), Modelling hydraulics and sediment transport at river confluences, in *River Confluences, Tributaries and the Fluvial Network*, edited by S. P. Rice, A. G. Roy, and B. L. Rhoads, pp. 17–32, John Wiley, Chichester, U. K.
- Biron, P. M., A. S. Ramamurthy, and S. Han (2004), Three-dimensional numerical modeling of mixing at river confluences, *J. Hydraul. Eng.*, 130(3), 243–253, doi:10.1061/(ASCE)0733-9429(2004)130:3(243).
- Boxall, J. B., and I. Guymer (2001), Estimating transverse mixing coefficients, *Proc. ICE*, 148(4), 263–275.
- Bradbrook, K. F., S. N. Lane, and K. S. Richards (2000), Numerical simulation of three-dimensional, time-averaged flow structure at river channel confluences, *Water Resour. Res.*, 36(9), 2731–2746, doi:10.1029/2000WR900011.
- Bradbrook, K. F., S. N. Lane, K. S. Richards, P. M. Biron, and A. G. Roy (2001), Role of bed discordance at asymmetrical river confluences, *J. Hydraul. Eng.*, 127(5), 351–368, doi:10.1061/(ASCE)0733-9429(2001)127:5(351).
- Constantinescu, G., A. Sukhodolov, and A. McCoy (2009), Mass exchange in a shallow channel flow with a series of groynes: LES study and comparison with laboratory and field experiments, *Environ. Fluid Mech.*, 9(6), 587–615, doi:10.1007/s10652-009-9155-2.
- Constantinescu, G., S. Miyawaki, B. Rhoads, A. Sukhodolov, and G. Kirkil (2011), Structure of turbulent flow at a river confluence with momentum and velocity ratios close to 1: Insight provided by an eddy-resolving numerical simulation, *Water Resour. Res.*, 47, W05507, doi:10.1029/2010WR010018.
- Constantinescu, G., S. Miyawaki, B. Rhoads, and A. Sukhodolov (2012), Numerical analysis of the effect of momentum ratio on the dynamics and sediment-entrainment capacity of coherent flow structures at a stream confluence, *J. Geophys. Res.*, 117, F04028, doi:10.1029/2012JF002452.
- Cruzado, A., Z. Velásquez, M. Pérez, N. Bahamón, N. S. Grimaldo, and F. Ridolfi (2002), Nutrient fluxes from the Ebro River and subsequent across-shelf dispersion, *Cont. Shelf Res.*, 22, 349–360, doi:10.1016/S0278-4343(01)00060-7.
- Durran, D. R. (1999), *Numerical Methods for Wave Equations in Geophysical Fluid Dynamics*, 1st ed., 465 pp., Springer, New York.
- Gaudet, J. M., and A. G. Roy (1995), Effect of bed morphology on flow mixing length at river confluences, *Nature*, 373(6510), 138–139.
- Gooseff, M. N., K. E. Bencala, and S. M. Wondzell (2008), Solute transport along stream and river networks, in *River Confluences, Tributaries and the Fluvial Network*, edited by S. P. Rice, A. G. Roy, and B. L. Rhoads, pp. 17–32, John Wiley, Chichester, U. K.
- Gualtieri, C. (2008), Numerical simulation of flow patterns and mass exchange processes in dead zones, paper presented at the 4th Biennial Meeting of iEMSs, UPC, Barcelona, Spain.
- Gualtieri, C., P. A. López-Jiménez, and J. M. Rodríguez (2009), A comparison among turbulence modelling approaches in the simulation of a square dead zone, paper presented at 33rd IAHR Congress: Water Engineering for a Sustainable Environment, IAHR, Vancouver, B. C.
- Heard, S. B., C. B. Gienapp, J. F. Lemire, and K. S. Heard (2001), Transverse mixing of transported material in simple and complex stream reaches, *Hydrobiologia*, 464, 207–218.
- Hodges, B. R., J. Imberger, A. Saggio, and K. B. Winters (2000), Modeling basin-scale internal waves in a stratified lake, *Limnol. Oceanogr.*, 45(7), 1603–1620, doi:10.4319/lo.2000.45.7.1603.
- Johannesson, H., and G. Parker (1988), Theory of river meanders, *Proj. Rep.* 278, Univ. of Minn., St. Anthony Falls Hydraul. Lab, Minneapolis, Minn.
- Kalkwijk, J. P. T., and R. Booij (1986), Adaptation of secondary flow in a nearly horizontal flow, *J. Hydraul. Res.*, 24(1), 19–37.
- Kiffney, P. M., C. M. Greene, J. E. Hall, and J. R. Davies (2006), Tributary streams create spatial discontinuities in habitat, biological productivity, and diversity in mainstem rivers, *Can. J. Fish. Aquat. Sci.*, 63(11), 2518–2530.

- Lane, S. N., D. R. Parsons, J. L. Best, O. Orfeo, R. A. Kostaschuk, and R. J. Hardy (2008), Causes of rapid mixing at a junction of two large rivers: Río Paraná and Río Paraguay, Argentina, *J. Geophys. Res.*, *113*, F02019, doi:10.1029/2006JF000745.
- Laraque, A., J. L. Guyot, and N. Filizola (2009), Mixing processes in the Amazon River at the confluences of the Negro and Solimões rivers, Encontro das Águas, Manaus, Brazil, *Hydrol. Processes*, *23*, 3131–3140, doi:10.1002/hyp.7388.
- Mellor, G. L., and T. Yamada (1974), Development of turbulence closure models for planetary boundary layers, *J. Atmos. Sci.*, *31*, 1791–1806.
- Muto, Y., H. Imamoto, and T. Ishigaki (2000), Velocity measurements in a straight open channel with a rectangular embayment, paper presented at 12th APD-IAHR: Sustainable Water Resources Management: Issues and Future Challenges for the Next Millennium, Bangkok, Thailand.
- Muto, Y., Y. Baba, and S. Aya (2002), Velocity measurements in open channel flow with rectangular embayments formed by spur dikes, in *Annals of Disaster Prevention Research Institute*, vol. 45B-2, Kyoto Univ., Kyoto, Japan.
- Parsons, D. R., J. L. Best, S. N. Lane, R. A. Kostaschuk, R. J. Hardy, O. Orfeo, M. L. Amsler, and R. N. Szupiany (2008), Large river channel confluences, in *River Confluences, Tributaries and the Fluvial Network*, edited by S. P. Rice, A. G. Roy, and B. L. Rhoads, pp. 17–32, John Wiley, Chichester, U. K.
- Prats, J., J. Armengol, R. Marcé, M. Sánchez-Juny, and J. Dolz (2010), Dams and reservoirs in the lower Ebro River and its effects on the river thermal cycle, *Handb. Environ. Chem.*, *13*, 77–95, doi:10.1007/698_2010_68.
- Ramón, C. L., A. Hoyer, J. Armengol, J. Dolz, and F. Rueda (2013), Mixing and circulation at the confluence of two rivers entering a meandering reservoir, *Water Resour. Res.*, *49*, 1429–1445, doi:10.1002/wrcr.20131.
- Rastogi, A. K., and W. Rodi (1978), Predictions of heat and mass transfer in open channels, *J. Hydraul. Div. Am. Soc. Civ. Eng.*, *104*(3), 397–420.
- Rhoads, B. L. (1996), Mean structure of transport-effective flows at an asymmetrical confluence when the main stream is dominant, in *Coherent Flow Structures in Open Channels*, edited by P. J. Ashworth et al., pp. 491–517, John Wiley, New York.
- Rhoads, B. L., and S. T. Kenworthy (1995), Flow structure at an asymmetrical stream confluence, *Geomorphology*, *11*, 273–293, doi:10.1016/0169-555X(94)00069-4.
- Rhoads, B. L., and S. T. Kenworthy (1998), Time-averaged flow structure in the central region of a stream confluence, *Earth Surf. Processes Landform*, *23*, 171–191, doi:10.1002/(SICI)1096-9837(199802)23:2<171::AID-ESP842>3.0.CO;2-T.
- Rhoads, B. L., and A. N. Sukhodolov (2001), Field investigation of three-dimensional flow structure at stream confluences: 1. Thermal mixing and time-averaged velocities, *Water Resour. Res.*, *37*(9), 2393–2410, doi:10.1029/2001WR000316.
- Rice, S. P., M. T. Greenwood, and C. B. Joyce (2001), Tributaries, sediment sources, and the longitudinal organization of macroinvertebrate fauna along river systems, *Can. J. Fish. Aquat. Sci.*, *58*(4), 824–840.
- Robson, B. J., and D. P. Hamilton (2004), Three-dimensional modelling of a *Microcystis* bloom event in the Swan River estuary, Western Australia, *Ecol. Modell.*, *174*, 203–222, doi:10.1016/j.ecolmodel.2004.01.006.
- Rodi, W. (2010), Large eddy simulation of river flows, paper presented at the International Conference of Fluvial Hydraulics (River Flow), IAHR-Fluvial Hydraulics Committee, Graunschwieg, Germany, Hampton, VA, USA.
- Roe, P. L. (1984), Generalized formulation of TVD Lax–Wendroff schemes, *ICASE Rep. 84-53*, NASA CR-172478, NASA Langley Res. Cent. Hampton, VA, USA.
- Rueda, F. J., and E. A. Cowen (2005), The residence time of a freshwater embayment connected to a large lake, *Limnol. Oceanogr. Methods*, *50*, 1638–1653.
- Rueda, F. J., and S. MacIntyre (2010), Modelling the fate and transport of negatively buoyant storm-river water in small multi-basin lakes, *Environ. Modell. Software*, *25*(1), 146–157, doi:10.1016/j.envsoft.2009.07.002.
- Rueda, F. J., S. G. Schladow, and S. Ó. Pálmarrsson (2003), Basin-scale internal wave dynamics during a winter cooling period in a large lake, *J. Geophys. Res.*, *108*(C3), 3097, doi:10.1029/2001JC000942.
- Smith, P. E. (2006), A semi-implicit, three-dimensional model of estuarine circulation, *Open File Rep. 2006-1004*, U.S. Geol. Surv., Sacramento, Calif.
- Sukhodolov, A., W. S. Uijttewaalt, and C. Engelhardt (2002), On the correspondence between morphological and hydrodynamical patterns of groyne fields, *Earth Surf. Processes Landform*, *27*, 289–305, doi:10.1002/esp.319.
- Sukhodolov, A. N., and T. Sukhodolova (2007), Coherent structures in river flows over submerged vegetation, in *Hydraulic Measurements and Experimental Methods*, edited by E. A. Cowen, pp. 172–177, Am. Soc. of Civ. Eng., Lake Placid, N. Y.
- Vidal, J., F. J. Rueda, and X. Casamitjana (2007), The seasonal evolution of high vertical-mode internal waves in a deep reservoir, *Limnol. Oceanogr. Methods*, *52*, 2656–2667.
- Vowinkel, B., I. Schnauder, and A. N. Sukhodolov (2007), Spectral dynamics of turbulence in shallow mixing layers at a confluence of two parallel stream, in *Hydraulic Measurements and Experimental Methods*, edited by E. A. Cowen, pp. 635–630, Am. Soc. of Civ. Eng., Lake Placid, N. Y.
- Weitbrecht, V., and G. Jirka (2001), Flow patterns and exchange processes in dead zones of rivers, paper presented at the IAHR Congress, Beijing.
- Zamani, K., F. A. Bombardelli, S. Wuertz, and P. E. Smith (2010), Toward a 3-dimensional numerical model of tidal currents in San Francisco Bay, in *Proceedings of the World Environmental and Water Resources Congress 2010*, pp. 1385–1394, Environ. and Water Resour. Inst., Am. Soc. of Civ. Eng., Providence, R. I.